High-density, Identified Cell Recordings from Motor Cortex of Awake Behaving Macaques using Multiple 1024-channel CMOS Probes

ANGOTZI, GN, BAKER, AME, VINCENZI, M, ORBAN, G, RIBEIRO, JF, TENORIO, Viviane, BERDONDINI, L and BAKER, SN

Citation:

ANGOTZI, GN, BAKER, AME, VINCENZI, M, ORBAN, G, RIBEIRO, JF, TENORIO, Viviane, BERDONDINI, L and BAKER, SN (2026). High-density, Identified Cell Recordings from Motor Cortex of Awake Behaving Macaques using Multiple 1024-channel CMOS Probes. IEEE Transactions on Biomedical Engineering. [Article]

This article has been accepted for publication in IEEE Transactions on Biomedical Engineering. This is the author's version which has not been fully edited and content may change prior to final publication. Citation information: DOI 10.1109/TBME.2026.3694160

High-density, Identified Cell Recordings from Motor Cortex of Awake Behaving Macaques using Multiple 1024-channel CMOS Probes

G.N. Angotzi, *Member*, *IEEE*, A.M.E. Baker, M. Vincenzi, *Member, IEEE,* G. Orban, J.F. Ribeiro, V. Tenorio, L. Berdondini*, *Member, IEEE,* S. N. Baker*

Abstract* — Objective/Background: Recording bioelectric signals from large populations of single neurons in the primate brain remains challenging. Chronic implants offer limited coverage (~100 channels) and sample fixed cortical regions, while acutely inserted electrodes allow broader access via multiple daily penetrations. We aimed to develop a CMOS-based probe with high electrode-channel density, and optimized procedures for acute large-scale single-unit recordings in behaving monkeys. Methods: We designed a novel single-shank SiNAPS CMOS probe for acute recordings in monkeys with additional integrated multiplexing circuits to reduce output lines. A multi-probe system enables synchronous sampling at 20 kHz/channel from two SINAPS-NHP probes during repeated insertions into the motor cortex of behaving macaques. We developed methods to identify neurons via antidromic activation. Results: The probe (10.7 mm × 158 µm × 50 µm) samples neural activity from 1,024 electrodes (14 × 14 µm², 30 µm pitch) arranged in four columns and reaches an electrode-channel density of 304.4 channels/mm2. A pilot hole facilitates dural penetration, and optimized insertion procedures allow recordings from diverse cortical sites. Some neurons were identified as pyramidal tract cells projecting to the spinal cord. Conclusion: Each probe enables monitoring of intracortical areas of 7.75 × 0.1 mm², detecting hundreds of single neurons per session, and reaches deep regions such as the anterior bank of the central sulcus, rich in corticospinal cells. Significance: This technology and methods unlock routine acute recordings from 2,048 channels with single-neuron resolution and cell-type identification, advancing the neurophysiological toolkit for primate research.

Index Terms— **Active pixel sensors, Microelectrodes, Neurotechnology, Electrophysiology, Neural implants**

I. INTRODUCTION

Neural recording technologies for large-scale, single-cell resolution in non-human primates (NHPs), particularly macaques, have seen significant advancements in recent years. While traditional microwire arrays have enabled pioneering long-term studies with recordings from >1,000 isolated units [1], achieving such yields using low-channel-count implants distributed across different brain areas typically requires many recording sessions. In contrast, recent CMOS-based high-density neural probes can achieve comparable or even higher yields per recording session. Moreover, multiprobe systems enable simultaneous monitoring across multiple brain regions, and can further enhance overall single-unit yield to support fine-grained electrophysiological and connectivity studies within localized and distributed brain circuits.

Originally developed for rodent studies, Neuropixels probes [2] have recently been adapted for use in NHPs, enabling high-density, large-scale recordings with single-neuron resolution [3]. The Neuropixels 1.0-NHP has three versions: short (960 electrodes over 10 mm shank length), medium (2,496 electrodes over 25 mm shank length) and long (4,416 electrodes over 45 mm shank length) [4]. However, all versions are limited to 384 simultaneous recording channels. These probes have permitted recordings of over 1,000 neurons using multiple shanks and are now increasingly used in cognitive and sensory neuroscience studies in macaques. A notable application is the Triple-N dataset [5], which used Neuropixels NHP-long probes to record from 27 subregions of the inferotemporal cortex while monkeys passively viewed 1,000 natural scene images. Such a dataset provides a rich resource for studying visual processing and cross-species comparisons with human data.

Another recent device is the NeuroScroll probe [6], a 1024-channel device with shank lengths ranging from 10 to 90 mm. It has demonstrated reliable chronic recordings in NHPs for up to 105 weeks. However, unlike Neuropixels, NeuroScroll requires external CMOS amplifiers and signal conditioning circuits, necessitating high-density interconnects (up to 179 channels/mm²). This increases assembly complexity and introduces experimental handling challenges.

Despite these advances, further progress is needed to enable the reliable acquisition of bioelectrical signals from large, distributed populations of individually identified neurons. This is essential for understanding the implementation and execution of brain functions. For example, motor cortical areas compute the sequence of activation required to produce a given movement. Multiple single unit recordings from these regions have great potential to discover the nature of these

This work was supported by BBSRC grant number BB/V00896X/1, NIH grant number R01NS119319, and an EU grant to the In2PrimateBrains consortium, number 956669.

G.N.A., M.V., G.O., J.F.R. and L.B. are with the Microtechnology for Neuroelectronics Unit, Fondazione Istituto Italiano di Tecnologia (IIT), Genova, Italy. A.M.E.B., V.T. and S.N.B. are with the Faculty of Medical Sciences, Newcastle University, Newcastle upon Tyne, NE2 4HH, UK. (co-correspondence e-mail: stuart.baker@ncl.ac.uk and luca.berdondini@iit.it).

This article has been accepted for publication in IEEE Transactions on Biomedical Engineering. This is the author's version which has not been fully edited and content may change prior to final publication. Citation information: DOI 10.1109/TBME.2026.3694160

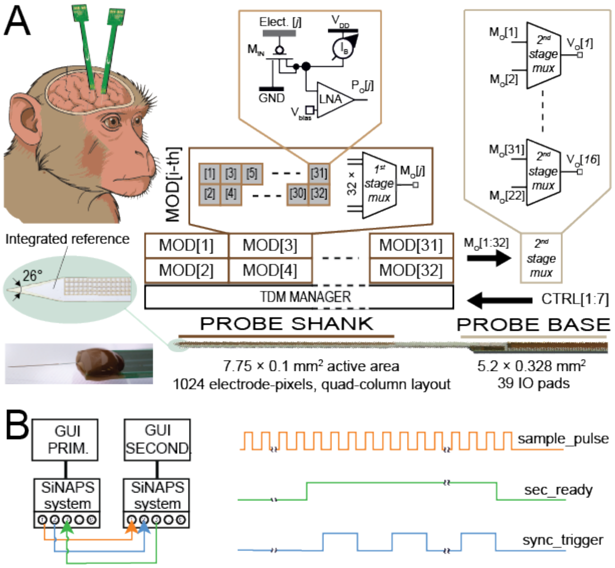

Fig. 1. Overview of the 1024 electrode-channels SiNAPS-NHP probe. (A) Illustration of multi-probe recordings in monkeys, with views of the realized probe, and schematic representations of the in-pixel analogue front-end (AFE), on-probe time-division-multiplexing (TDM) and 2nd stage multiplexing (MUX) circuits. (B) Schematics and control signals for synchronous recordings from 2048 electrode-channels using two SiNAPS-NHP probe systems.

computations [7]. Important insights can be obtained by identifying which cells relay the cortical output to subcortical centers. The most prominent motor cortical output neurons are the corticospinal cells. These project long axons through the pyramidal tract at the medulla, and thence on to the spinal cord where they synapse with spinal cord interneurons and, uniquely in primates, to the motoneurons which ultimately relay all motor commands to muscles [8].

Interestingly, pyramidal tract neurons (PTNs) can be straightforwardly identified by antidromic stimulation [9]. This approach involves implanting stimulating electrodes in the pyramidal tract (PT) at the medulla. The placement of the stimulation electrode is performed while monitoring an epidural recording over the motor cortex; it is fixed at the location with the lowest threshold to elicit an antidromic field potential. In subsequent recording sessions, PTNs will respond to PT stimulation with an antidromic spike.

Several criteria can be used to confirm that an evoked spike is antidromic. It should have a low temporal jitter – typically less than 0.1 ms. Larger jitters suggest a synaptic response, produced from collaterals of unrecorded PTNs activating the recorded cell. Secondly, there should be a sharp threshold, with an all-or-none single neuron response appearing over a narrow range of stimulus intensity (typically ~20 µA). Finally, the response should show collision with spontaneous spikes. Because an action potential leaves in its wake a region of refractory axon, when spontaneous and antidromic spikes meet in the axon between the stimulating and recording electrodes they cannot pass and no antidromic spike is seen in the cortical recording. This occurs when the spontaneous spike occurs over a narrow window around the timing of the PT stimulus.

To advance the current ability to identify a large number of distributed single neurons individually, here we adapted this approach for identifying PTNs and developed a novel high-channel count CMOS probe system based on the SiNAPS technology [10], [11], specifically designed to enable multiple acute recordings in the motor cortical areas of awake behaving monkeys (Fig. 1). Specifically, the realized SiNAPS-NHP probe supports continuous sampling from 1024 electrode channels with a compact I/O interface that delivers real-time broadband electrophysiological data at 20 kHz/channel. This overcomes limitations in the number of recording channels of current Neuropixels probes, in reducing the overall probe area and thus in the electrode-channel density of the probe. Further, the acquisition system was designed to support up to 2,048 synchronous channels using multiple probe systems. To overcome limitations of chronic implants like the Utah Array (~100 channels, small, fixed region of the cortex at a fixed depth), we established procedures for repeated acute insertions through the dura. This allows daily targeting of different cortical sites, thus expanding the spatial coverage and flexibility of recordings.

II. METHODS

A. CMOS Probe Design and Realization

A single-shank, high-density CMOS neural probe featuring 1024 electrode channels was developed based on the SiNAPS circuit architecture. This architecture already demonstrated its efficiency for *in vivo* neural recordings [10], [11]. In this design, we modified the electrode-pixel layout, and the architecture was enhanced with additional multiplexing circuits to halve the number of signal outputs, thereby simplifying integration on narrow printed circuit boards (PCBs), see Fig. 1A.

The probe integrates multiple functional modules along a single, elongated shank. Each module contains 32 electrode-pixel sensors, where each pixel comprises a metal electrode pad of 14 x 14 µm^2 (on the top CMOS metal layer) for neural signal detection, along with underlying signal amplification and conditioning circuits. Consistent with previous SiNAPS designs, each pixel features a DC-coupled analogue front-end (AFE) with a two-stage low-noise amplifier (LNA) and a periodically enabled feedback loop to manage DC offset at the electrode-tissue interface (Fig. 1A). While the amplifier operates primarily in open-loop mode, the autozeroing loop is periodically activated to adjust the bias current of the first stage dynamically, stabilizing the DC operating point.

To streamline data routing, each module employs a 32:1 time-division multiplexing (TDM) scheme, with buffered outputs directed toward the probe base. In this implementation, the main amplifier delivers 40 dB AC gain and incorporates a first-order low-pass filter with a 4 kHz cutoff to minimize aliasing in the TDM stream.

Unlike standard SiNAPS probes, which stream data out on one channel per 32-electrode module, the SiNAPS-NHP probe uses analog double data rate (DDR) transmission to stream two samples in the same time slot; this enables full-array readout of 1,024 channels while minimizing the number of I/O pads, avoiding the need for a larger probe base that would increase fabrication costs. To limit crosstalk and signal degradation at

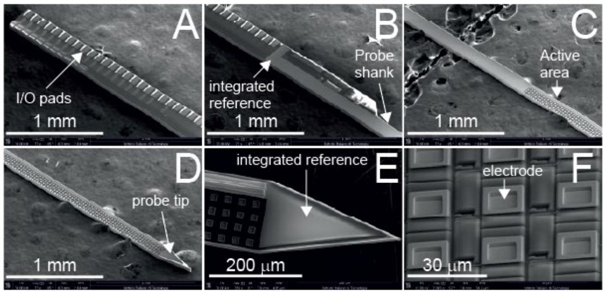

Fig. 2. SEM pictures of the realized SiNAPS-NHP active neural probes. The device was realized with a very narrow base to facilitate experimental use. (A) Top of the probe base with the I/O pads. (B) Interface between the probe base and shank with the integrated reference I/O pad. (C) Probe shank with the beginning of the active area. (D) Probe tip. (E) Close-up view of the probe tip with integrated reference. (F) Close-up view of the electrode-pixels.

this additional 2:1 TDM stage, buffering was used at both the input and output, while switching elements were designed as pass transistors (to minimize charge injections and clock feedthrough effects), with Ron << Roff. Finally, since this second multiplexing occurs after amplification, its input-referred noise contribution is expected to be negligible, preserving high-fidelity neural recordings.

To assess potential parasitic effects introduced by the DDR-based multiplexing stage, we evaluated cross-correlation in recorded neural data as an indirect indicator of possible coupling. Conventional crosstalk measurements (based on independently driving a source line and observing its effect on another line) were not feasible without additional post-processing steps to electrically connect selected electrodes for signal injection. Instead, we analyzed cross-correlations in the action potential (AP) band, where spatial correlation of neural signals is typically limited to nearby electrodes recording the same unit activity. Correlation patterns across electrodes, both within and between adjacent modules, were then compared to differentiate biological correlations from potential circuit-induced coupling.

Ultimately, this architecture leads to a ≈ 4.6-fold reduction in the base area of the 8-shank SiNAPS probe previously reported [11]. The recording area comprises 2 × 16 functional modules arranged along the shank, forming a 4 × 256 electrode-pixel array with a 30 µm pitch, totaling 1024 channels, each consuming 6 µW of DC power. This layout expands the lateral field of view while maintaining a compact cross-sectional profile suitable for implantation.

Devices were realized in standard 180 nm CMOS technology and post-processed to define the probe shape and electrode material by adapting previously presented processes [11], [12], [13]. The microstructuring of the CMOS substrate allowed us to achieve probe shank dimensions of 158 µm x 10.7 mm (active area covered by the electrodes 7.77 × 0.107 mm^2) and probe base dimensions of 328 µm × 5.2 mm, leading to an electrode-channel density of 304.4 channels/mm^2. The native 10 × 10 μm^2 opening on the top CMOS insulator layer – which exposes the top CMOS metal layer (an Al/Cu metal alloy) at each electrode site – was patterned with a 14 × 14 μm^2 square structured with platinum (Pt) lift-off [12]. By taking advantage of the same lift-off step, an integrated Pt pseudo-reference was patterned next to the electrodes (close-up views in Fig. 2B and 2E). After a dry-etching process to pattern the probe shape and thickness, the SiNAPS-NHP probes were released by backside grinding until reaching a thickness of 50 µm. Fig. 2 shows SEM pictures of the realized devices. Following experimental validation of the initial prototypes, SiNAPS-NHP probes were realized at wafer-level by Corticale Srl (Genoa, Italy).

The probe was then mounted on a narrow PCB (6 mm wide, 1 mm thick, and 5 cm long) and wire bonded. The PCB layout was optimized to allow flexible positioning, enabling access to any point within the exposed craniotomy inside the cranial chamber while also enabling the optional use of the integrated pseudo-reference. Successively, Pt was electrodeposited onto the electrodes to reduce their electrochemical impedance and, consequently, the related noise contribution. Electrodeposition was performed using a potentionstat/galvanostat (PGSTAT204, Autolab Metrohm, Switzerland) with a three electrode electrochemical cell consisting of an Ag/AgCl reference electrode, a Pt counter electrode and the microelectrodes as working electrode. It has to be noted that, while individual microelectrode access is not possible in this circuit, an analog switch bypasses the electrode-pixel circuit to enable parallel access, using all electrodes as a single working electrode. Prior to electrodeposition, the Pt microelectrodes were cleaned in 0.5 mol/l (1 N) sulfuric acid (H_2SO_4) by cyclic voltammetry (CV) to ensure uniformity. The same cell configuration was then used for Pt electrodeposition by replacing the electrolyte with "Platinum AP + 4G/L Pt" solution (Technic, Italy), and by applying a constant average current of 10 nA per electrode for 1 hour.

B. *Data Acquisition System*

The data acquisition (DAQ) platform is built around an FPGA development board based on the Altera Cyclone IV (ZEM4310, OpalKelly Inc., USA), and, besides power management circuits for stable, low-noise supply from a 5 V input, it also integrates a bank of 32 12-bit, high-speed, low-power SAR ADCs (MAX11105, Maxim Integrated, USA). The MAX11105 was selected to match the system requirements, digitizing 64 channels per ADC at 20 kSamples/s with 12-bit resolution (input-referred VLSB ≈ 5.86 µV), sufficient for extracellular electrophysiology. This off-probe ADC architecture was chosen as a practical compromise: it saves circuit area to keep the probe base laterally compact, shifts a significant fraction of power dissipation away from the tissue, and accelerates system validation, whereas a fully integrated on-probe quantizer would increase on-shank power, complexity, and thermal constraints. The FPGA handles time-division multiplexed data readout and digitization and runs a customized real-time digital processing unit (DPU) that manages probe operation and implements a pipelined, real-time second-order IIR filter with a programmable high-pass cutoff (2 Hz or 300 Hz) and a fixed 5 kHz low-pass cutoff (Cortical srl, Italy). For real-time PC interfacing, the FPGA supports high-speed data transfer via CameraLink (raw and processed data) and low-speed command/control via UART.

This article has been accepted for publication in IEEE Transactions on Biomedical Engineering. This is the author's version which has not been fully edited and content may change prior to final publication. Citation information: DOI 10.1109/TBME.2026.3694160

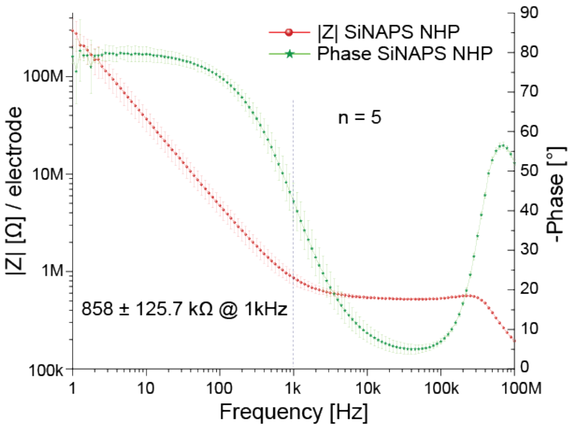

Fig. 3. Electrochemical Impedance Spectroscopy (EIS) of the electrodeposited Pt microelectrodes. The mean impedance module at 1 kHz was 858 ± 125.7 kΩ/electrode (n = 5 probes * 1024 electrodes).

Two synchronized DAQ systems are used (Fig. 1B) to acquire data from 2048 electrode channels of two SiNAPS-NHP probes. As previously anticipated, for each DAQ, data is acquired frame by frame, with each frame consisting of 1,024 channels read out using a time-division multiplexing (TDM) and double data rate (DDR) scheme. The beginning of each frame is defined by the rising edge of a common *sample_pulse* signal operating at 20 kHz, which is generated by the primary system upon being enabled via the primary GUI. The primary system is enabled first, initiating data acquisition. The same s*ample_pulse* is then sent to the secondary system, which responds by asserting the *sec_ready* signal and starting its own acquisition. Since both systems share the same *sample_pulse*, their frame acquisitions are inherently synchronized. Additionally, a *sync_trigger* signal generated by the primary and recorded by both systems is used during offline processing to precisely align the two data streams. Finally, each DAQ connects to the corresponding probe via a 1-meter, 50-way cable (P.N. SQCD-025-36.00-TBL-TED-1-S, Samtec, USA). A compact board integrated at the distal side of the cable ensures low-noise delivery of the nominal 1.8 V supply and common reference bias voltages.

C. Surgical Implant

Experimental recordings have been conducted to date in five macaque monkeys (two male; weight 6.4-12.7 kg). In all cases, animals first underwent an MRI scan under general anesthesia (2-3% sevoflurane inhalation), which allowed the generation of a 3D model of the skull. This was used to produce a digital implant design, based on the annular headpiece first described by [14]. The headpiece was an annular ring (width 8-10 mm); the ring shape allowed fixation to bone, while the central area remained clear to allow access to brain structures. The headpiece was shaped to fit the skull surface, and incorporated a chamber positioned over the primary motor cortex (M1) and dorsal premotor cortex (PMd) (internal dimensions 18x18 mm^2). The final design was 3D printed in titanium and coated in hydroxyapatite to enhance osteointegration. It was implanted under general anesthesia (2-3% sevoflurane inhalation with 12 μg/kg/hour alfentanil by intravenous infusion), using the system of expanding head bolt assemblies to attach the headpiece firmly to the skull also described by [14]. These consisted of a disc (diameter 13 mm), and an expansion bolt which could grip a hole inside the disk. Four 4 mm holes were drilled in the skull to align with slots placed in the headpiece. Further, 13 mm craniotomies were made near to these holes. A 13 mm steel disc was then placed in each craniotomy and maneuvered under the skull to lie under the nearby 4 mm hole. The expanding bolt was then placed through this hole, and expanded to grasp the 13 mm disc. The headpiece was then placed over the four protruding bolts, and nuts used to fix the headpiece firmly to the skull. This system allowed the mechanical load to be distributed widely, above the skull, on the large annular headpiece, and beneath the skull on the four 13 mm diameter discs. This reduced loading provided a highly stable, long-lasting implant. Electromyogram (EMG) electrodes were implanted over 12 muscles in the arm in the same surgery, with wires tunneled subcutaneously to a connector placed on the headpiece. After recovery from the surgery, a craniotomy was opened in the chamber in a further brief surgery under anesthesia to provide daily access for penetrations into the brain. In this surgery, we also implanted two parylene insulated tungsten electrodes (LF501G, Microprobes Inc, Gaithersburg, MD, USA) into the PT at the medulla for stimulation [15], [16].

D. Pre-Processing and Data Analysis

The recorded data were preprocessed using a custom application developed in MATLAB called SpikeLAB, which provides functionalities such as data visualization in both time and frequency domains, filtering, “bad channel” characterization, common average referencing (CAR), and single unit sorting. As individual electrodes cannot be accessed separately for electrochemical characterization in this architecture, standard electrochemical criteria for identifying “bad channels” cannot be applied [17], [18]. Channel reliability was therefore assessed directly from the recorded signals, accounting for the operation of the front-end circuitry. For each channel, data was first filtered in the action potential (AP) band and the signal RMS was then computed over the recording and used as a quality metric. Channels with RMS values within 0.5× to 1.3× the median RMS across all channels were considered reliable and included in the analysis. Channels with RMS below this range typically indicate amplifier saturation, while higher RMS values are associated with excessive noise; both conditions reflect failure of the autozeroing loop to establish a correct operating point such as in case of poor electrode–tissue coupling. Sorting was finally performed by accessing in SpikeLAB the open-source MATLAB implementation of Kilosort [19]. No manual curation was performed, but a minimum mean firing rate (MFR) threshold was set. Finally, we extracted recording quality indicators, such as i) the signal RMS for each channel, ii) the number of masked channels, and iii) the number of units.

E. Antidromic Identification with SiNAPS-NHP Probes

Once a probe had been inserted into the final location within the cortex, we began by recording responses to PT stimulation, at a fixed intensity chosen to be above threshold for most PTNs (typically 500 μA). PT stimuli were given as biphasic chargebalanced pulses, width 0.1 ms per phase (stimulator model 2100, AM Systems Inc, Sequim, WA, USA). Stimuli were given with a period of 0.5-0.7 s; recordings continued for two minutes. Following this, the PT stimulation was turned off, and recordings made of spontaneous activity during behavioral task performance, typically lasting around one hour. At the end of the session, a further two-minute recording of responses to pyramidal tract (PT) stimulation was made.

To improve the visual distinction between field potentials and antidromic spike responses to PT stimulation, we calculated re-referenced responses *x'* as follows:

$$x'_i(t) = x_i(t) - \big(x_{i-16}(t) + x_{i+16}(t)\big)/2 \qquad (1)$$

Where *i* is the channel number, *t* is recording time, and *x* is the original recorded data. Because the SiNAPS-NHP probes have four columns of contacts, the offset of 16 channels is equivalent to subtracting the average of the channel four rows above and four rows below from every signal. We expect fields to change slowly with depth, whereas PTN spikes should have a narrowly restricted spatial extent. Spikes should therefore be better visible in *x'* than *x*.

Usually, the problem of spike sorting is carried out in a blind manner – first detecting how many different neurons contribute to the recording and then separating spikes and classifying them. The problem of discriminating identified PTNs is different, since we know *a priori* what the target spike waveform looks like from the antidromic response, in this case across multiple channels. We approached the problem of identifying these spikes by generating a multi-dimensional filter which can be passed over the data to reconstruct the spike train [20], [21]. We model the data by assuming that there is an underlying spike train $S(t)$, where $S(t)=1$ if a spike occurs at time t and $S(t)=0$ otherwise (t is discrete time, indexing the sample number). If the vector $x_i(t)$ represents the signal from channel $i=1\ldots M$ of the probe, we extend this by a factor K so that the new MK x 1 vector $X(t)$ contains samples from all M channels, over a range of K lags backwards in time from t:

$$X(t)=[x_1(t), x_1(t-1)\ldots x_1(t-K+1), x_2(t)\ldots x_M(t-K+1)]^{\mathrm{T}} \qquad (2)$$

Assuming the occurrence times of a small number of detected spontaneous spikes are t_j (j=1..J), then the average spike waveform expressed in the extended vector format described above is:

$$Y = \frac{1}{J}\sum_{j=1}^{J} X(t_j) \qquad (3)$$

The covariance matrix of the recorded data is defined as:

$$C = E(X(t)X^T(t)) \qquad (4)$$

where E(•) is the expectation operator. The spike filter is calculated as:

$$F = Y^T C^{-1} \qquad (5)$$

The estimate of the spike train S(t) is provided by:

$$\hat{S}(t) = FX(t) \qquad (6)$$

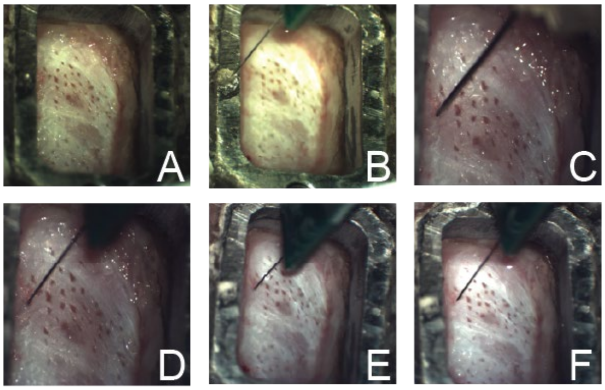

Fig. 4. Photographs of recording chamber and sequence of penetration. (A) View of the chamber with exposed dura. (B) SiNAPS-NHP probe located over a piece of Spongostan foam placed over a fiducial mark on the chamber. (C) A 30G needle placed over the intended penetration site over the dura. (D) SiNAPS-NHP probe after penetration through the dura. (E) SiNAPS-NHP probe at final depth for recording. (F) SiNAPS-NHP probe after removal from cortex.

III. RESULTS

A. Characterization of SiNAPS-NHP Probes

The impedance of the electrodes (Fig. 3) was measured in NaCl 0.9% using the setup described for Pt electrodeposition. To estimate the microelectrode impedance, a known source of noise for recordings, individual microelectrode measurements were not possible with the circuits of this CMOS-probe. Instead, the total impedance of the 1024 short-circuited electrodes was measured and multiplied by the number of electrodes, yielding an average impedance of 858 ± 126 kΩ at 1 kHz per electrode (mean ± SD over n = 5 probes; 1024 electrodes/probe).

The overall RMS noise (electrode and circuit) was evaluated in saline using a Pt wire to ground the solution (n = 5 probes x 1024 electrodes). The measured noise was: 22.3 ± 6.4 μV_{RMS} for the full-band [0.1 - 5000 Hz], 19.2 ± 7.2 μV_{RMS} for the LFP-band [0.1 – 300 Hz], and 10.5 ± 1.4 μV_{RMS} for the AP-band [300 – 5000 Hz].

These measured noise values reflect the architectural choice of integrating a single full-band analog front end directly beneath each electrode site within the implantable shank, under stringent area and power constraints. This design philosophy aligns with the concept of fully immersible neural probes, in which the entire recording chain is embedded within the implantable structure. A representative example is given by the 192-channel architecture proposed in [22], where reported noise values are comparable to those measured here (from 11.22 to 16.29 µVrms in the AP band depending on the size of the electrodes), but rely on serial data transmission schemes that pose scaling challenges for channel counts on the order of 1,024 as proposed in our work. In contrast, for Neuropixels probes [2], [4], [23], the amplification and conditioning circuits are placed at the probe base, outside the implantable shank, and with the number of simultaneously recorded channels being smaller than the total number of available electrodes, such that recordings are limited to a selectable subset of sites in each experimental trial. This architectural choice permits to relax area and power constraints thus enabling lower electronic noise (down to 7.44 µVrms in the AP band for Neuropixels 2.0) at the cost of larger per-channel area (0.001 mm²) and power budgets (22 µW/channel) that would be impractical to integrate directly beneath each electrode site. Finally, NeuroSeeker [24] which targets full-array readout of 1,356 channels, reports 12.4 µVrms in the AP band and 50.2 µVrms in LFP, with 0.09 mm² silicon area per channel and 45 µW/channel power consumption.

B. Penetration of SiNAPS-NHP Probes into Macaque Cortex

The use of SiNAPS-NHP probes in awake behaving monkeys required us to overcome several technical challenges. The first is the space occupied by the printed circuit board (PCB) which is used to make connections to the silicon probe. When positioned in a recording chamber, the PCB limits how close to the chamber edge the probe can penetrate. For this reason, an important design specification was that the PCB should be as narrow as possible (final width 6 mm). Additionally, we have found that it is essential to visualize the penetration of the probe to avoid breakages. This is aided by a

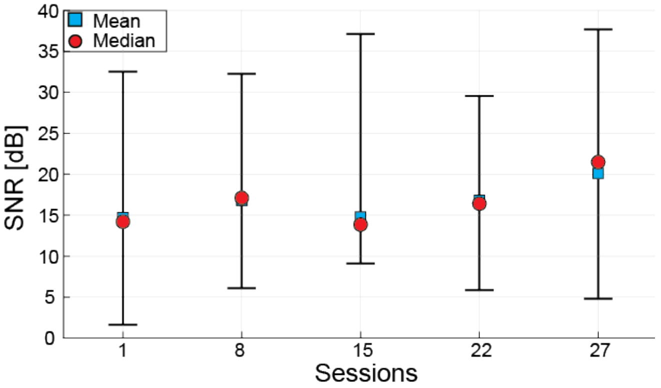

Fig. 5. SNR progression over 27 acute recording sessions, demonstrating the stability of recording performance across repeated insertions using the same probe. For each session, the SNR range is represented by a bar plot, considering all units. The mean and median values are represented by blue squares and red circles, respectively.

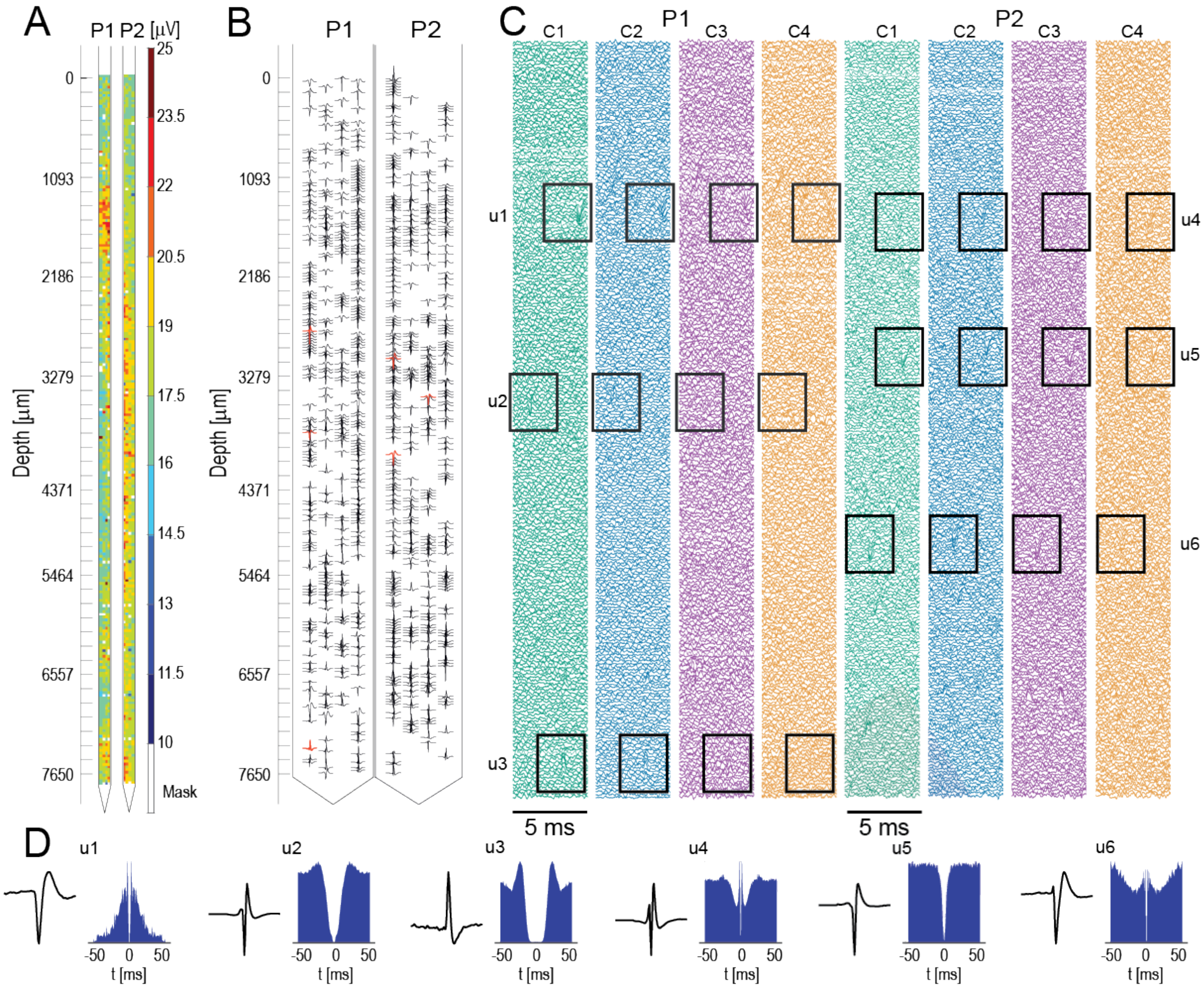

Fig. 6. Example of dual SiNAPS NHP probe synchronous recordings for a total of 2048 electrode-channels in the NHP motor cortex. Signals were filtered in the AP band (300 Hz to 5 KHz) and CAR was performed. A total of 35 (over 1024) bad channels (i.e. not at correct working point) were masked in Probe1, and 21 were masked in Probe2. In (A), we represent the channels' RMS for a time window of 5 ms. In (B), we represent the templates of the single units extracted by Kilosort-3 with an MFR of at least 0.1 spike/s in Probe1 (n=587) and Probe2 (n=725), with SNRs of 12.4 dB (P1) and 9.6 dB (P2). Three sample units are highlighted in red for each probe. (C) shows a close-up of the signals recorded by the 4 columns (C1-4) of electrodes for each probe. Black boxes highlight the sample units identified in (B). (D) shows the templates and autocorrelograms for each of the sample units displayed in (B) and (C).

low profile recording chamber design as in [9].

Penetration of a thin probe through the dura mater is difficult. When the dura mater is exposed by a craniotomy inside a recording chamber, there is rapid tissue growth, and it becomes thick and tough. This can be prevented using the anti-mitotic agent 5-fluorouracil (5-FU) [9], [25], coupled with meticulous dural care. Tissue growth must be removed daily using fine instruments and visualization under an operating microscope – this is again assisted by the low-profile chamber design. With such care, it is possible to maintain the dura in a thin state for many months, but even with these measures we found that SiNAPS-NHP probes would not penetrate readily into the cortex.

To overcome this issue, the probe was attached to a stereotaxic manipulator mounted on the solid metal plate to which the animal's head was fixed using the headpiece. This allowed accurate movement of the probe in three dimensions. The probe was angled at 30 degrees to the vertical, so that it penetrated the dura approximately perpendicularly.

In between the probe and the stereotaxic manipulator, we used a microdrive (Nan instruments, Nof HaGalil, Israel), which allowed fine control of probe depth. The probe was positioned over a fiducial mark on the side of the chamber, and the manipulator readings noted (Fig. 4). We found that placing the probe directly on the metal chamber mark frequently led to breakages. We therefore placed a small piece of hemostatic sponge soaked in saline (Spongostan, Johnson & Johnson) over the mark (Fig. 4B). The soaked sponge was translucent, so that the mark could still be seen. With the sponge in place the moment when the probe contacted the surface could be easily visualized, with less risk of probe breakage.

The desired penetration site within the chamber was then calculated relative to the fiducial marker. This used a map of the chamber on which previous penetrations were plotted, and the estimated location of the central sulcus based on the MRI. The manipulator was adjusted to the calculated coordinates, and the probe lowered onto the dura. This location was noted visually, and the probe was raised and moved away. A hand-held 30-gauge needle was then used to make a small puncture at the identified site on the dura (Fig. 4C). Care was taken to angle this needle parallel to the intended probe penetration, and not to pass into the cortex. We found holding the needle by hand more effective than mounting the needle in a manipulator. Using a manipulator, the needle would often dimple the dura, and then suddenly penetrate some distance and damage cells in superficial cortical layers. Such penetrations therefore yielded poor superficial cell recordings. By contrast, the additional visual and proprioceptive feedback available when holding the needle by hand allowed the needle to be rapidly retracted once penetration had been achieved. The photographs in Fig. 4 show the dura covered in small scars caused by previous such penetrations.

The probe was then returned to the intended penetration site, and advanced through the dural hole using the gross height adjustment of the stereotaxic manipulator (Fig. 4D). We found this preferable to using the microdrive, as with manual adjustment of the probe height any failure to penetrate led to clear probe bending; the probe could then be retracted. By contrast, with slow penetration controlled by the microdrive bending was hard to detect and eventually led to breakage. If a probe failed to penetrate, it was removed and a further needle puncture made. We had the impression that this was often due to a failure to pass through not the dura, but the arachnoid underneath. This could also be punctured with a second attempt with the needle and thereby allow penetration. Typically, in successful penetrations the probe was advanced 1-1.5 mm below the surface of the dura.

The probe was then advanced slowly (5-10 μm/s) to the desired recording depth using the microdrive. We found that advancing slowly improved the yield of cells and also reduced drift during recordings. Macaque M1 has a sub-region on the brain surface ('Old M1' in the terminology of [26]); when recording here, the probe typically was advanced only 1.5-3 mm (Fig. 4E). When penetrating the part of M1 within the central sulcus ('New M1'), we could use the full length of the probe and advance 7.7 mm. It is important to note that with this procedure it was less important to place the probe precisely in a given location, as to know where it was eventually placed.

Once the probe was at the final depth, recordings were commenced while the monkey performed the behavioral task, which differed depending on the project. Task performance was monitored by single or multi-channel force transducers (3 monkeys), or by high-speed video (2 monkeys). In all cases, a mixture of analog and digital task signals needed to be recorded together with EMG from 12 muscles, as well as the signals from the 1024 contact SiNAPS-NHP probes. This was achieved using an Intan RHD2000 recordings system (Intan Technologies, Los Angeles, CA, USA) running in parallel with the SiNAPS data acquisition device. To synchronize signals for off-line analysis, digital pulses coding task events were sampled by both devices. In some sessions, two SiNAPS-NHP probes were penetrated simultaneously into the cortex. These were connected to two independent SiNAPS data acquisition systems; again, by recording identical task digital events to these as well as the Intan card, the different data streams could be synchronized off-line. Using the workflow described above, we found that probe breakages for dual probe insertions became

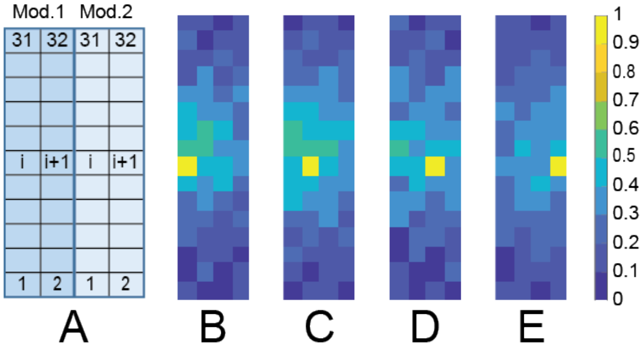

Fig. 7: Cross-correlation–based assessment of DDR-induced effects on in vivo recorded data: (A) DDR scheme, where the i-th electrodes of two adjacent modules are read simultaneously; (B)–(E) cross-correlation maps of four representative electrodes within the same row (self-correlation highlighted in yellow) with respect to all electrodes in the two adjacent modules. The observed correlations reflect the expected spatial overlap of neural activity due to dense electrode sampling, with no indication of systematic correlation patterns attributable to parasitic coupling from the TDM or DDR circuitry.

rare once good practices were established. As illustrated in Fig. 5, a single SiNAPS probe was reused for up to 27 consecutive acute recording sessions, with the signal-to-noise ratio (SNR) remaining stable across sessions, indicating robust probe performance under repeated acute use. Future developments in automated surgical procedures, outside the scope of this work, may further increase probe reusability and experimental reliability.

C. Electrophysiological SiNAPS probe recordings

The data presented in this section were filtered within the 300 Hz to 5 kHz frequency range. Bad channels were masked, and CAR was applied before single units were detected using Kilosort3 with a minimum MFR threshold of 0.1 spikes/s. Out of the 2048 available electrodes, 35 channels (CHs) were masked in Probe1 (P1), and 21 were masked in Probe2 (P2). Figure 6A shows the RMS of the channels computed over a 5 ms time window coinciding with evident neural activity. The higher RMS values correspond to higher spiking activity in the corresponding brain regions. Figure 6B shows the templates of the single units extracted by Kilosort-3 with a firing rate above the threshold, numbering 587 in P1 and 725 in P2. Three single units were selected as a sample for the results presented below and are highlighted in red. To provide a detailed picture of the

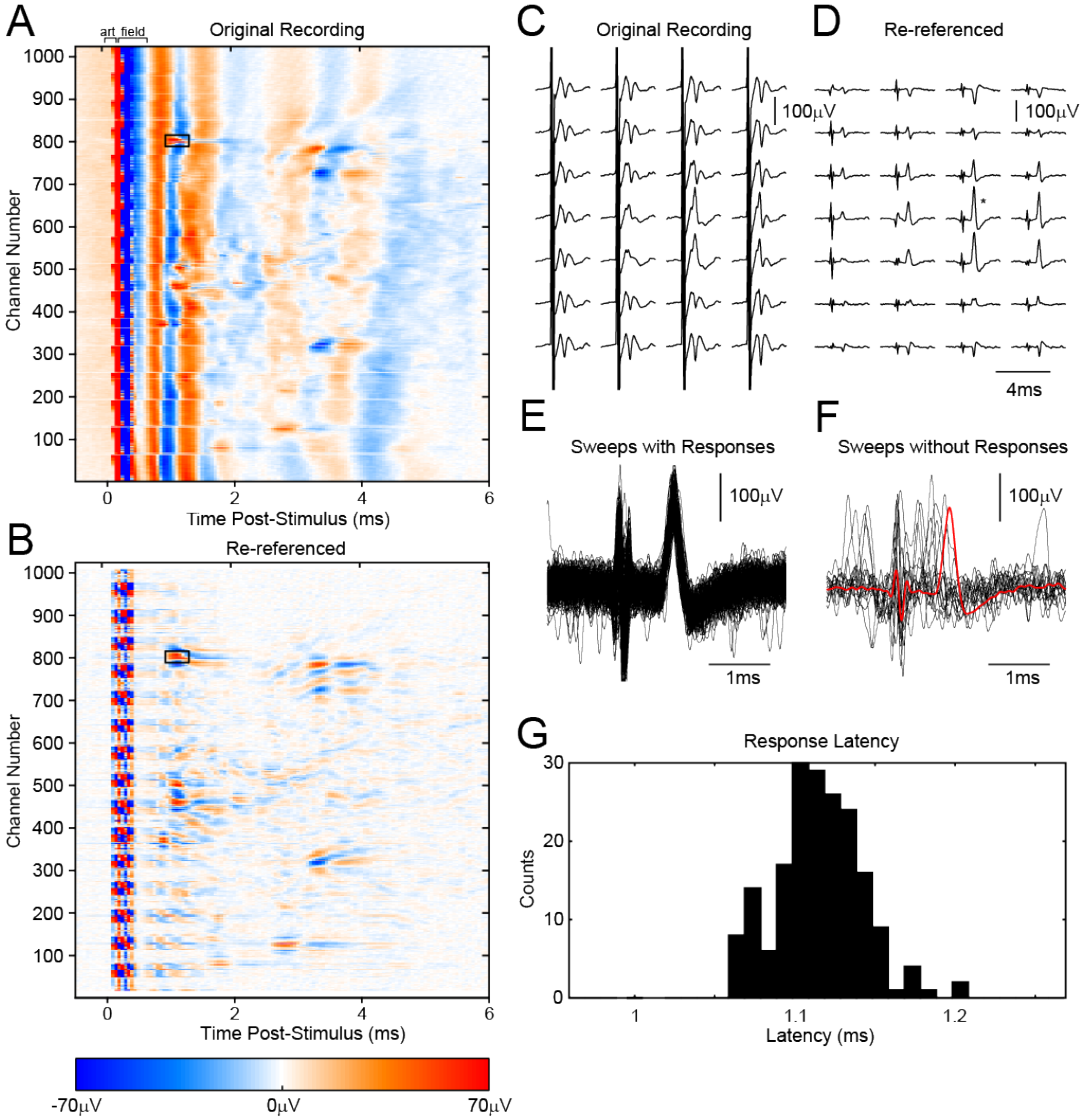

Fig. 8. Recording with a SiNAPS-NHP probe of antidromic responses evoked by pyramidal tract (PT) stimulation. A, false color map showing the average response of each channel of a 1024-channel SiNAPS-NHP probe following PT stimulation. An initial stimulus artifact ('art') is followed by a field potential ('field'). Superimposed on this field on some channels are antidromic spike responses. Low channel numbers are deeper within the tissue. B, sweeps as (A), but re-referenced as described in the text. The stimulus artifact was reduced in duration, and the field abolished, allowing antidromic spikes to be more easily visualized. (A) and (B) are shown on the same color scale. C, D, average responses following PT stimulation for the channels indicated by the black box in (A, B). Sweeps are arranged according to the relative geometrical arrangement of the channels. (C) shows original recorded data as in (A), (D) shows re-referenced data as in (B). E, overlain single sweeps for the channel marked by * in (D), for the 187/202 sweeps with a response around 1.1 ms after the stimulus. F, as (E), but for the 15/202 sweeps with no response around 1.1 ms. Overlain red trace shows the average of responses in (E) for comparison. G, histogram of the latency of the spike peak for responses in (E).

This article has been accepted for publication in IEEE Transactions on Biomedical Engineering. This is the author's version which has not been fully edited and content may change prior to final publication. Citation information: DOI 10.1109/TBME.2026.3694160

neuronal activity recorded in regions with higher RMS values, Fig. 6C shows a close-up of the AP signals recorded by the two probes. Each column of electrodes is shown independently, and the signals corresponding to the sample units selected in Fig. 6B are highlighted in black boxes. Finally, Fig. 6D visualizes the templates and autocorrelograms for each sample unit identified in Figs. 6B and 6C. The median SNR for P1 and P2 is of 12.4 dB and 9.6 dB.

In addition, to investigate potential parasitic effects associated with the DDR-based multiplexing, we analyzed cross-correlation in the AP band between electrodes read through the shared DDR output. As direct crosstalk measurements were not feasible (section II.A), this approach provides an indirect assessment of possible coupling. Figs. 7(B)–(E) show the correlation maps for four representative electrodes within the same row across two representative adjacent modules. While a non-zero correlation is expected due to the spatial proximity of electrodes sampling APs from the same unit, the observed correlation distributions exhibit a clear spatial decay consistent with biological origin. No anomalous correlation peaks attributable to the TDM or DDR circuitry were observed, indicating that the multiplexing scheme does not introduce significant parasitic coupling and preserves signal integrity.

D. *Antidromic Identification of Pyramidal Tract Neurons*

Offline analysis began by compiling averages of the responses to PT stimulation for each SiNAPS channel and displaying these using a false color map (Fig. 8A) on which the abscissa shows time post-stimulus, and the ordinate channel number. Channel numbers increase with distance from the probe tip, so that the y axis approximately corresponds to the recording location. The large stimulus artifact is immediately apparent (‘art’, Fig. 8A); this is followed by a field potential response (‘field’, Fig. 8A). It is difficult to distinguish any antidromic PTN spikes from this field.

Figure 8B shows the average of the re-referenced signal, in which potentials with shallow spatial gradient are removed. Several responses are revealed in this display. One, marked by a black box, is illustrated in more detail in the rest of Fig. 8. While field and spikes are confusingly superimposed in the average of the original data across channels (Fig. 8C), the spike is revealed clearly in the re-referenced data (Fig. 8D).

Fig. 8CD shows average responses; Fig. 8EF shows superimposed single sweeps for the single channel with the largest putative spike response (channel marked by * in Fig. 8D). For this panel, the recording has been reconstructed by convolving the data sampled at 20 kHz with a sinc function [27]. This provides a high-resolution view of the spike. In most sweeps, there was a clear response (Fig. 8E); however, on 15/202 sweeps, there was no response at the usual latency (compare traces in Fig. 8F with the overlain red trace, which shows the average of the responses from Fig. 8E). In these sweeps, a spontaneous spike occurred before the antidromic latency, leading to collision of the antidromic response. Figure 8G presents a histogram of the spike peak latency for the responses of Fig. 8E. There was extremely low jitter (standard deviation only 27 μs), consistent with an antidromic response.

To detect the spike times of spontaneous spikes produced by the PTN, we first detected the times of a small number of spontaneous spikes at the start of the recording using threshold crossing on the channel with the largest spike in the antidromic response. We selected waveforms similar in shape and size to the antidromic spike by requiring that they pass through voltage windows set manually. Figure 9A presents an average of the antidromic (red) and spontaneous (black) spikes, for the same cell as illustrated in Fig. 8. The close similarity seen in Fig. 9A, coupled with the observed collisions between spontaneous and antidromic spikes (Fig. 8F), provides a high degree of confidence that antidromic and spontaneous spikes come from one and the same neuron.

Figure 9B shows a brief section of recording from the probe channel with the largest spontaneous spike for the cell shown in Fig. 9A. Figure 9C shows the reconstructed pulse train $\hat{S}(t)$; peaks in this waveform were detected (MATLAB “findpeaks” function) and are marked by red circles. The pulse train has a SNR 2.2x higher than the single channel recording (SNR calculated as spike height divided by noise SD, 13.9 vs 6.3, or 22.86 dB vs. 15.99 dB). The improvement in SNR obtained by combining multiple channels together optimally has been described previously [28].

E. *Correcting for Electrode Drift*

Extracting the occurrence times of spontaneous PTN spikes is straightforward using the approach described above if recordings are stable. However, when making recordings with SiNAPS-NHP probes lasting around one hour in awake behaving monkeys, we frequently observed drift, where the signals moved vertically up the probe. This probably corresponded to the brain tissue adjacent to the probe relaxing gradually after the mechanical stress of driving the probe down. An example of this is shown in Fig. 10. A PTN was clearly

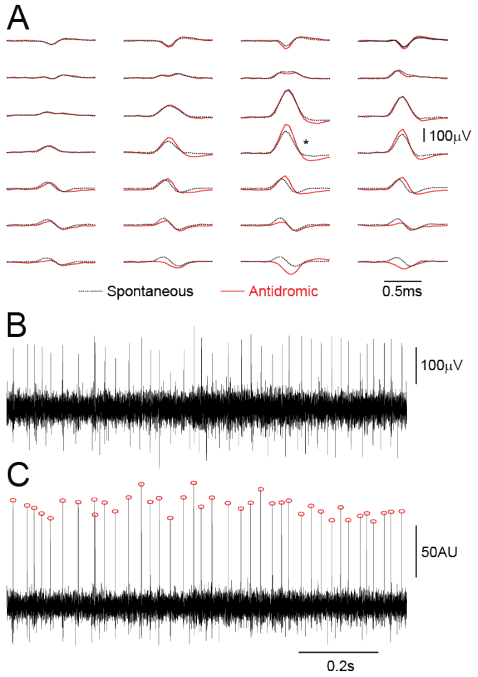

Fig. 9. Extracting spontaneous firing of antidromically identified pyramidal tract neuron. (A) Overlain averages of the antidromic spike waveform of the cell shown in Fig. 6 (red), and the spike waveform of a spontaneously active cell (black). The close similarity across channels provides confidence that these are generated by the same neuron. (B) example 1s-long recording from the channel with the largest spike (* in A). (C) example pulse waveform extracted with the multi-channel spike filter. Detected peaks are marked with red circles.

visible in the antidromic responses gathered at the start of the experiment (Fig. 10A); one hour later the same cell was also clearly visible (based on its antidromic latency and waveshape across channels), but it had shifted around five rows higher along the probe (Fig. 10B).

To account for such drift, we assumed that the spike waveshape does not change, but that it was merely translated by an integer number of rows up or down the probe. We recalculated a range of filters for different shifts and extracted the corresponding pulse train estimates $\hat{S}(t)$. Figure 10C plots the heights of the peaks of the pulse train for various shifts. At the start of the recording, the pulse train with no shift had peaks which were clearly separated from the noise (Fig. 10C, red box); selecting these heights extracted a clean single unit, with consistent waveform (Fig. 10D, red). The inter-spike interval histogram (Fig. 10E, red) showed a lack of intervals within the first 1 ms, consistent with the neuronal refractory period. At around 611 s into the recording, a sudden change occurred, and the peak height at zero shift reduced. However, peaks remained clearly separated from the noise in the pulse train extracted by shifting one row up the probe (Fig. 10D, green), allowing continued clean discrimination. At 823 s after the recording

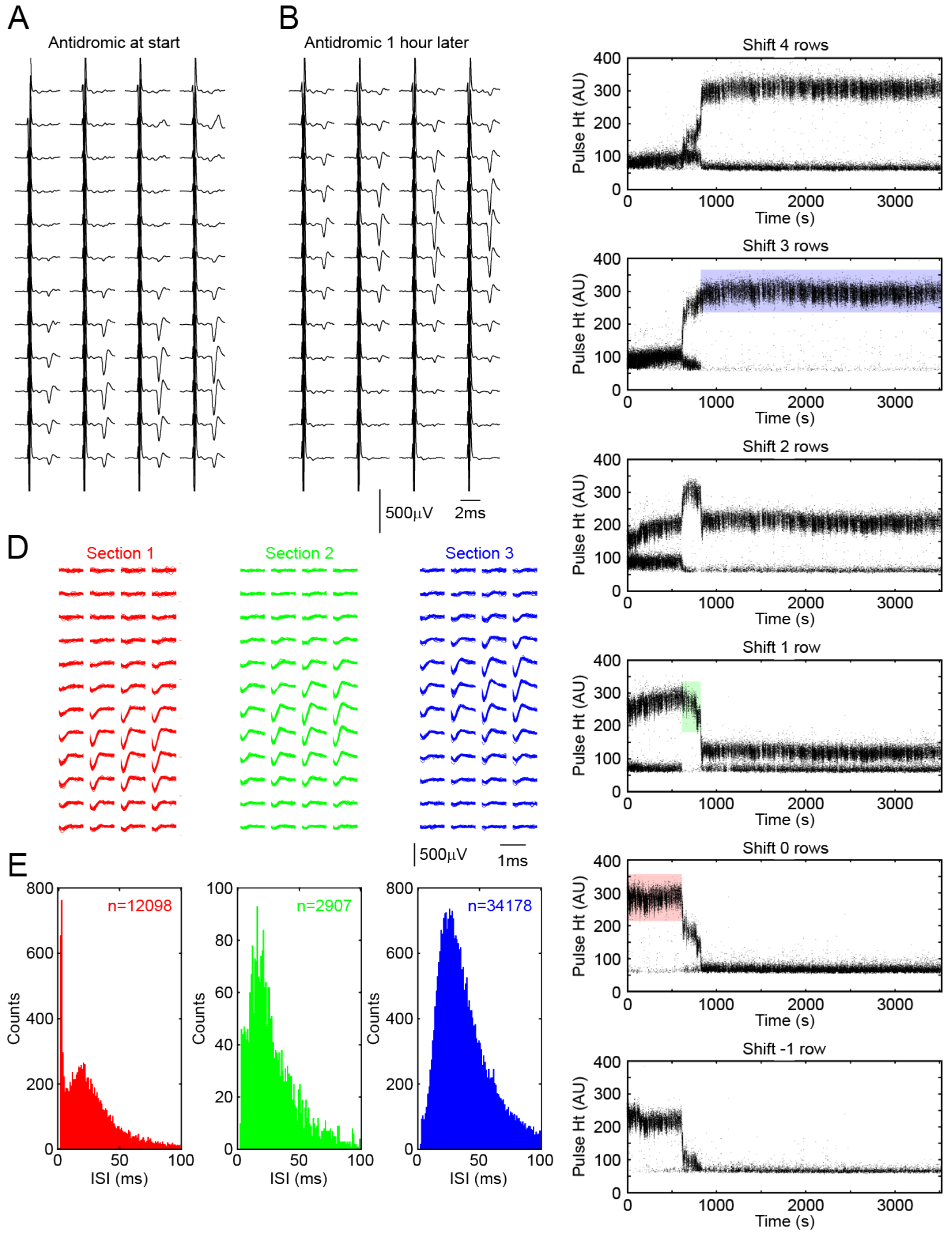

Fig. 10. Detecting and tracking drift over a long recording. Average antidromic responses recorded (A) at the start of a session, and (B) at the end one hour later. Note the clear drift in the channel on which the antidromic spike can be seen. (C) Height of peaks in the pulse waveform (corresponding to red circles in Fig. 9) for the entire recorded period. Each plot shows the results when applying the spike filter shifted by several rows up (positive shift) or down (negative shift) relative to the original channels on which the antidromic spike was seen. Sudden shifts in pulse height correspond to movements between probe and tissue. The recording was divided into three sections, and pulses selected from no shift (red, section 1), shift of +1 row (green, section 2) and +3 row (blue, section 3). (D) spike waveforms and (E) interspike interval histograms, for the corresponding color-coded sections. Waveform displays for (A, B, D) show the same channel numbers.

start, there was another change, which necessitated shifting a further two rows up the probe (Fig. 10E, blue). The inter-spike interval histograms over these three sections were broadly consistent, although the first section showed a narrow peak at an interval of 3 ms reflecting burst firing which was not seen in the other two. This may be caused by damage to the neuron and its dendritic tree shortly after probe penetration, leading to injury discharges; we assume that after the damaged neuron membrane resealed these injury discharges ceased.

The total shift required to discriminate the pulse train from the beginning to the end of the file was three rows, although equally good separation could be achieved with a shift of four rows (Fig. 10C, top). This compares with an estimated five row shift based on antidromic response in Fig. 10B. It is possible that some additional shift occurred between the end of the recording of task-related activity and the start of the second file measuring antidromic responses. In between these two files, the monkey typically makes multiple postural adjustments after the long period of focused task performance. It is therefore highly plausible that there could be an additional movement of tissue relative to probe at this time.

IV. CONCLUSION

To advance the state-of-the-art in recording and identifying large populations of single neurons in the cerebral cortex of awake, behaving monkeys, we demonstrated a novel high-channel-count SiNAPS-NHP probe. This slender probe offers 1024 electrode-channels over a total (shank and base) Si area of 3.4 mm^2, leading to an electrode-channel density (i.e. number of recording channels over total Si area) of 304.4 channels/mm^2. This is ≈43-fold higher than current Neuropixels-NHPs probes that reach 6.4-7 channels/mm2 depending on the layout. Integrated with a multiprobe recording system, simultaneous acquisition from 2,048 electrodes (2 probes x 1024 electrodes) is possible, capturing sub-millisecond neural signals from 7.75×0.1 mm^2 recording areas with 30 µm electrode pitch. We also report procedures for routine multiple acute insertions, allowing broad spatial coverage, and methods for antidromic identification of a subset of recorded neurons. Identifying which neurons project to specific output regions, such as the spinal cord in the case of M1, is crucial for understanding the computational roles of cortical circuits. Although, as in Neuropixels-NHP, on-probe integration of custom digital communication circuits may further reduce the number of data outputs at a cost of higher on-probe power consumption, and longer shanks would allow deeper brain areas to be reached, the SiNAPS-NHP system already represents a significant advance in the neurophysiological toolkit for cortical primate research. In the future, the slender base could be exploited to mount the probe into cannulas, thereby extending its length and enabling access to deeper brain structures.

ACKNOWLEDGMENT

We thank Terri Jackson and Andrew Atkinson for animal training, Rocio Palacios-O'Connor for veterinary support, Michelle Waddle for surgical theatre nursing, and Norman Charlton for mechanical engineering support. We would like also to thank Corticale Srl (Italy) for having scaled up the fabrication of the SiNAPS 1024 NHP probes and for their support on the firmware.

REFERENCES

[1] D. A. Schwarz et al., "Chronic, wireless recordings of large-scale brain activity in freely moving rhesus monkeys," Nat Methods, vol. 11, no. 6, pp. 670–676, Jun. 2014, doi: 10.1038/nmeth.2936.

[2] J. J. Jun et al., "Fully integrated silicon probes for high-density recording of neural activity," Nature, vol. 551, no. 7679, pp. 232–236, Nov. 2017, doi: 10.1038/nature24636.

[3] E. M. Trautmann et al., "Large-scale high-density brain-wide neural recording in nonhuman primates," Nat Neurosci, vol. 28, no. 7, pp. 1562–1575, Jul. 2025, doi: 10.1038/s41593-025-01976-5.

[4] "Neuropixels-NHP." Accessed: Oct. 31, 2025. [Online]. Available: https://www.neuropixels.org/probes-nhp

[5] Y. Li et al., "Triple-N Dataset: Non-human Primate Neural Responses to Natural Scenes," May 11, 2025. doi: 10.1101/2025.05.06.652408.

[6] Y. Liu et al., "A high-density 1,024-channel probe for brain-wide recordings in non-human primates," Nat Neurosci, vol. 27, no. 8, pp. 1620–1631, Aug. 2024, doi: 10.1038/s41593-024-01692-6.

[7] K. V. Shenoy, M. Sahani, and M. M. Churchland, "Cortical Control of Arm Movements: A Dynamical Systems Perspective," Annu Rev Neurosci, vol. 36, no. 1, pp. 337–359, Jul. 2013, doi: 10.1146/annurev-neuro-062111-150509.

[8] R. N. Lemon and J. Griffiths, "Comparing the function of the corticospinal system in different species: Organizational differences for motor specialization?," Muscle Nerve, vol. 32, no. 3, pp. 261–279, Sep. 2005, doi: 10.1002/mus.20333.

[9] S. N. Baker et al., "Multiple single unit recording in the cortex of monkeys using independently moveable microelectrodes," J Neurosci Methods, vol. 94, no. 1, pp. 5–17, Dec. 1999, doi: 10.1016/S0165-0270(99)00121-1.

[10] G. N. Angotzi et al., "SiNAPS: An implantable active pixel sensor CMOS-probe for simultaneous large-scale neural recordings," Biosens Bioelectron, vol. 126, no. September 2018, pp. 355–364, Feb. 2019, doi: 10.1016/j.bios.2018.10.032.

[11] G. N. Angotzi et al., "Multi-Shank 1024 Channels Active SiNAPS Probe for Large Multi-Regional Topographical Electrophysiological Mapping of Neural Dynamics," Advanced Science, vol. 12, no. 16, Apr. 2025, doi: 10.1002/advs.202416239.

[12] J. F. Ribeiro, F. Boi, A. Lecomte, G. N. Angotzi, and L. Berdondini, "Bioelectrodes for high-channel count and small form factor CMOS neural probes," in 2021 10th International IEEE/EMBS Conference on Neural Engineering (NER), IEEE, May 2021, pp. 388–391. doi: 10.1109/NER49283.2021.9441160.

[13] J. F. Ribeiro et al., "Channels, Layout and Size Scalability of Implantable CMOS-Based Multielectrode Array Probes," in 2022 International Electron Devices Meeting (IEDM), IEEE, Dec. 2022, pp. 29.6.1-29.6.4. doi: 10.1109/IEDM45625.2022.10019384.

[14] Roger. Lemon and A. Prochazka, Methods for neuronal recording in conscious animals. London, UK: Wiley, 1984.

[15] I. S. Glover and S. N. Baker, "Both Corticospinal and Reticulospinal Tracts Control Force of Contraction," The Journal of Neuroscience, vol. 42, no. 15, pp. 3150–3164, Apr. 2022, doi: 10.1523/JNEUROSCI.0627-21.2022.

[16] J. A. Tapia, T. Tohyama, A. Poll, and S. N. Baker, "The Existence of the StartReact Effect Implies Reticulospinal, Not Corticospinal, Inputs Dominate Drive to Motoneurons during Voluntary Movement," The Journal of Neuroscience, vol. 42, no. 40, pp. 7634–7647, Oct. 2022, doi: 10.1523/JNEUROSCI.2473-21.2022.

[17] S. F. Cogan, "Neural Stimulation and Recording Electrodes," Annu Rev Biomed Eng, vol. 10, no. 1, pp. 275–309, Aug. 2008, doi: 10.1146/annurev.bioeng.10.061807.160518.

[18] J. R. Abbott et al., "Planar amorphous silicon carbide microelectrode arrays for chronic recording in rat motor cortex," Biomaterials, vol. 308, p. 122543, Jul. 2024, doi: 10.1016/j.biomaterials.2024.122543.

[19] M. Pachitariu, S. Sridhar, J. Pennington, and C. Stringer, "Spike sorting with Kilosort4," Nat Methods, vol. 21, no. 5, pp. 914–921, May 2024, doi: 10.1038/s41592-024-02232-7.

[20] J. Škarabot et al., "Decoding firings of a large population of human motor units from high-density surface electromyogram in response to transcranial magnetic stimulation," J Physiol, vol. 601, no. 10, pp. 1719–1744, May 2023, doi: 10.1113/JP284043.

[21] A. Francic and A. Holobar, "On the Reuse of Motor Unit Filters in High Density Surface Electromyograms Recorded at Different Contraction Levels," IEEE Access, vol. 9, pp. 115227–115236, 2021, doi: 10.1109/ACCESS.2021.3104762.

[22] R. Willaredt, C. Grandauer, D. De Dorigo, M. Kuhl, and Y. Manoli, "A 0.00175 mm 2 and 9.62 µ W per Channel Direct-Digitization Front End With EDO Compensation for Neural Probes With a Spatial Resolution of 35 µ m," IEEE J Solid-State Circuits, vol. 60, no. 7, pp. 2330–2340, Jul. 2025, doi: 10.1109/JSSC.2025.3555007.

[23] S. Wang et al., "A Compact Quad-Shank CMOS Neural Probe With 5,120 Addressable Recording Sites and 384 Fully Differential Parallel Channels," IEEE Trans Biomed Circuits Syst, vol. 13, no. 6, pp. 1625–1634, Dec. 2019, doi: 10.1109/TBCAS.2019.2942450.

[24] B. C. Raducanu et al., "Time Multiplexed Active Neural Probe with 1356 Parallel Recording Sites," Sensors, vol. 17, no. 10, p. 2388, Oct. 2017, doi: 10.3390/s17102388.

[25] R. L. Spinks, S. N. Baker, A. Jackson, P. T. Khaw, and R. N. Lemon, "Problem of Dural Scarring in Recording From Awake, Behaving Monkeys: A Solution Using 5-Fluorouracil," J Neurophysiol, vol. 90, no. 2, pp. 1324–1332, Aug. 2003, doi: 10.1152/jn.00169.2003.

[26] J.-A. Rathelot and P. L. Strick, "Subdivisions of primary motor cortex based on cortico-motoneuronal cells," Proceedings of the National Academy of Sciences, vol. 106, no. 3, pp. 918–923, Jan. 2009, doi: 10.1073/pnas.0808362106.

[27] A. V. . Oppenheim, A. S. . Willsky, and S. Hamid. Nawab, Signals & systems. Harlow, UK: Prentice Hall, 1997.

[28] P. G. Musial, S. N. Baker, G. L. Gerstein, E. A. King, and J. G. Keating, "Signal-to-noise ratio improvement in multiple electrode recording," J Neurosci Methods, vol. 115, no. 1, pp. 29–43, Mar. 2002, doi: 10.1016/S0165-0270(01)00516-7.